ADVANCED ENERGY MATERIALS

www.advenergymat.de

Defect-Engineered Ultrathin δ-MnO_2 Nanosheet Arrays as Bifunctional Electrodes for Efficient Overall Water Splitting

Yunxuan Zhao, Chao Chang, Fei Teng, Yufei Zhao, Guangbo Chen, Run Shi, Geoffrey I. N. Waterhouse, Weifeng Huang, and Tierui Zhang**

Recently, defect engineering has been used to intruduce half-metallicity into selected semiconductors, thereby significantly enhancing their electrical conductivity and catalytic/electrocatalytic performance. Taking inspiration from this, we developed a novel bifunctional electrode consisting of two monolayer thick manganese dioxide (δ-MnO_2) nanosheet arrays on a nickel foam, using a novel in-situ method. The bifunctional electrode exposes numerous active sites for electrocatalytic rections and displays excellent electrical conductivity, resulting in strong performance for both HER and OER. Based on detailed structure analysis and density functional theory (DFT) calculations, the remarkably OER and HER activity of the bifunctional electrode can be attributed to the ultrathin δ-MnO_2 nanosheets containing abundant oxygen vacancies lead to the formation od Mn^{3+} active sites, which give rise to half-metallicity properties and strong H_2O adsorption. This synthetic strategy introduced here represents a new method for the development of non-precious metal Mn-based electrocatalysts for eddicient energy conversion.

Growing energy demand, coupled with concerns about fossil fuel depletion and anthropogenic greenhouse gas emissions, motivates the search for clean and sustainable technologies for electricity generation and the production of energy carriers such as H_2.[1] Electrochemical water splitting is widely considered as one of the most attractive future technologies for H_2 production, due to its simplicity and reasonably high energy conversion efficiency.[2] However, water splitting is a thermodynamically unfavorable process, with the overall efficiency of the process hindered somewhat by the large overpotentials for the hydrogen evolution reaction (HER) and oxygen evolution reaction (OER) on most electrocatalyst materials. Currently, Pt and IrO_2 are the most efficient electrocatalyst for HER and OER, respectively. However, their widespread use for industrial scale water splitting is not practical due to the high cost and scarcity of Pt and Ir. Therefore, it is highly desirable to develop efficient low-cost electrocatalysts based on earth-abundant elements for overall water splitting. Recently, ultrathin 2D layered materials have attracted extensive attention in electrocatalysis,[3] photoconversion,[4] ferromagnetism,[5] and thermocatalysis,[6] owing to their unique electronic structures.[7] Layered materials with a thickness of one or a few atomic layers, such as graphene,[8] g-C_3N_4,[9] and MoS_2,[10] show very promising performance for HER and OER mainly due to their tunable electronic structure.[11] As a means of further enhancing the electronic properties and performance of such 2D materials, researchers are increasing focusing on defect engineering (vacancy or facet controlling) and exploitation of structure–property–performance relationships.[12] Through defect engineering, the electronic structure of many semiconductors can be modified significantly, in extreme cases transforming semiconductors with the low intrinsic electrical conductivity into materials with half-metallicity. The large improvement in electrical conductivity realized through defect engineering can lead to remarkable enhancements in catalytic and electrocatalytic performance.

Layered manganese dioxide (δ-MnO_2), consisting of edge-sharing MnO_6 octahedra, demonstrates very good oxygen evolution reaction and oxygen reduction reaction performance and has been widely investigated in relation to these processes.[13] However, δ-MnO_2 has generally been considered inactive for HER, due to its unsuitable electronic structure and low conduction band level.[14] Recently, single-layer MnO_2 nanosheets doped with Mn and O vacancies (V_{Mn} and V_o) were found to

Y. Zhao, C. Chang, Prof. F. Teng
Jiangsu Engineering and Technology Research Center
of Environmental Cleaning Materials (ECM)
School of Environmental Science and Engineering
Nanjing University of Information Science & Technology
Nanjing 100084, P. R. China
E-mail: tfwd@163.com

Y. Zhao, Dr. Y. Zhao, G. Chen, R. Shi, Prof. T. Zhang
Key Laboratory of Photochemical Conversion
and Optoelectronic Materials
Technical Institute of Physics and Chemistry
Chinese Academy of Sciences
Beijing 100190, P. R. China
E-mail: tierui@mail.ipc.ac.cn

Prof. G. I. N. Waterhouse
School of Chemical Sciences
The University of Auckland
Auckland 1142, New Zealand

Dr. W. Huang
College of Engineering
Peking University
Beijing 100871, P. R. China

The ORCID identification number(s) for the author(s) of this article can be found under https://doi.org/10.1002/aenm.201700005.

DOI: 10.1002/aenm.201700005

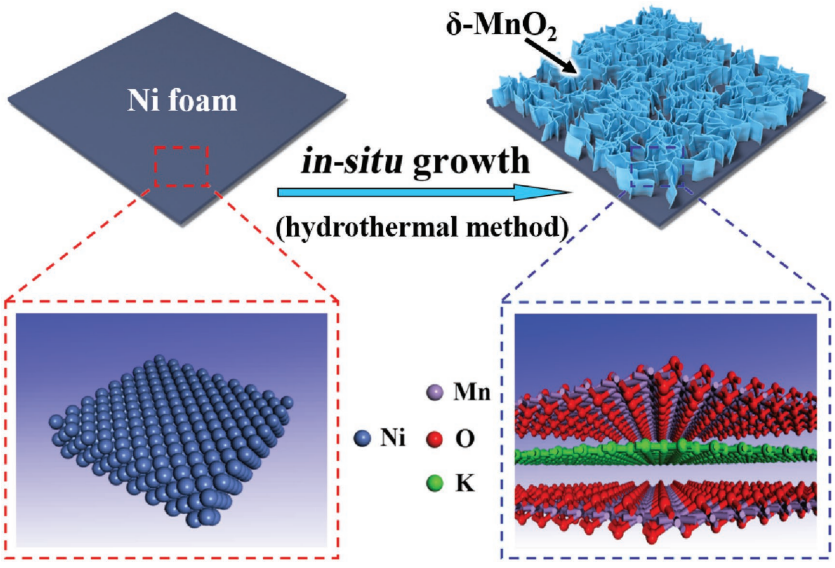

Scheme 1. Schematic showing the in situ growth of ultrathin δ-MnO_2 nanosheets on an Ni foam (NS-MnO_2).

contain half-metallic character, a property not shared by their bulk counterparts,[12a] providing a tantalizing new strategy for improving the electronic properties and conductivity of δ-MnO_2 for overall water splitting.

Herein, ultrathin δ-MnO_2 nanosheet arrays of only two-monolayer thickness (1.4 nm) were successfully prepared via a novel one-step in situ growth process on the surface of an Ni foam (denoted as NS-MnO_2) (**Scheme 1**). The NS-MnO_2 exhibited excellent electrocatalytic performance for both HER and OER with low overpotentials of 197 and 320 mV at 10 mA cm^{-2}, and Tafel slopes of 62 and 40 mV dec^{-1}, respectively. Based on detailed structure analyses and density functional theory (DFT) calculations, the remarkably OER and HER activity can be attributed to the unique structure of the nanosheets which contain an abundance of V_o and associated Mn^{3+} active sites, with the latter directly confirmed by X-ray absorption near-edge structure spectroscopy (XANES). The formation of Mn^{3+} active sites introduces half-metallicity into the nanosheets whilst V_o promotes H_2O adsorption, thereby enhancing the overall water splitting performance. This defect-engineering strategy represents a viable approach for the large-scale development of non-precious metal Mn-based electrocatalysts for efficient electrical-to-chemical energy conversion.

NS-MnO_2 was prepared by a facile one-step hydrothermal treatment of Ni foam (denoted as NF) in the presence of aqueous $KMnO_4$, with the color of foam changing from silver to black during the hydrothermal treatment (Figure S1A, Supporting Information). The X-ray diffraction (XRD) pattern of the sample obtained by sonication of NS-MnO_2 in ethanol showed four main peaks, confirming the successful formation of δ-MnO_2 on NF (JCPDS 86-0666) (Figure S1B, Supporting Information), with an interlayer spacing of ≈0.7 nm calculated from the (00*l*) reflections. Quantitative energy dispersive X-ray (EDX) analysis examined the elemental composition of NS-MnO_2 (Figure S2, Supporting Information). Elements identified in the sample were Ni, Mn, K, and O, with the atom ratio K:Mn being 0.397 (the K was likely intercalated between the δ-MnO_2 layer).

Scanning electron microscopy (SEM) confirmed that NS-MnO_2 consisted of an irregular array of 2D MnO_2 nanosheets aligned almost vertically on the surface of the NF (**Figure 1**A), in contrast to the starting Ni foam had a smooth morphology (Figure S1C, Supporting Information). The morphology of the δ-MnO_2 nanosheets was also investigated using transmission electron microscopy (TEM). As shown in Figure 1B, the δ-MnO_2 nanosheets had warped edges and thicknesses ≈1.5 nm, corresponding to two monolayers along the (001) direction. The lattice spacing of 0.245 nm, corresponding to the (101) plane of δ-MnO_2, was clearly observed in the high-resolution TEM (HRTEM) image (Figure 1C). The corresponding selected-area electron diffraction (SAED) pattern confirmed the polycrystalline nature of the nanosheets, and well-defined diffraction rings can readily be indexed to the (006) and (101) planes of δ-MnO_2 (inset of Figure 1C). The thickness of δ-MnO_2 nanosheets determined by atomic force microscopy (AFM) was ≈1.5 ± 0.1 nm, in good accord with the TEM findings (Figure 1D,E). EDX maps obtained during the TEM measurements confirmed a uniform spatial distribution of K, Mn, and O elements in the ultrathin δ-MnO_2 nanosheets (Figure 1F). Bulk δ-MnO_2 particles (denoted as Bulk-MnO_2) synthesized by thermal decomposition of $KMnO_4$ in air, were phase pure by XRD with a mean size of ≈3.0 µm by TEM (Figure S3A,B, Supporting Information). Electrochemical reaction centers are mainly located on the surface of catalysts.[15] Accordingly, the ultrathin δ-MnO_2 nanosheets were expected to offer a much higher concentration of active sites and thus superior electrocatalytic performance compared to Bulk-MnO_2, an aspect we explore in detail below.

X-ray absorption fine structure (XAFS) was applied to explore the local atomic structure and the defect sites in NS-MnO_2. As shown in **Figure 2**A, the Mn K-edge XANES spectra and the corresponding extended X-ray absorption fine structure (EXAFS) *k*-space spectra of Bulk-MnO_2 and NS-MnO_2 were similar, except that the absorption edge of NS-MnO_2 was shifted by about 0.5 eV to lower energy, indicating a slightly lower oxidation state of Mn in NS-MnO_2 compared with Bulk-MnO_2. Furthermore, analysis of the pre-edge region of the XAFS *k*-space spectra for Bulk-MnO_2 and NS-MnO_2 provided further useful information about the Mn oxidation state in these materials (Figure S4, Supporting Information). Two peaks can be observed for Bulk-MnO_2. In comparison, only one broad peak was found for NS-MnO_2, with the position of the peak intermediate between the two peaks of Bulk-MnO_2. The shift of the peak to lower energy indicates a lower average Mn oxidation state in NS-MnO_2 due to defect engineering. The above results confirm that the coexistence of Mn (III) and Mn (IV) in NS-MnO_2.[16] The different local atomic arrangements around Mn atoms in NS-MnO_2 and Bulk-MnO_2 were displayed in the corresponding k-space (Figure 2B) and R-space spectra

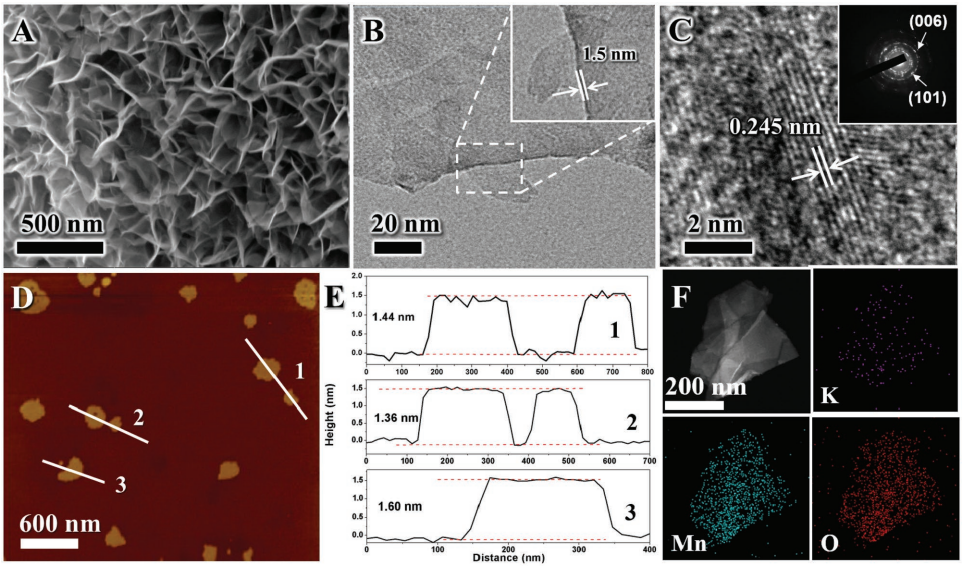

Figure 1. A) SEM image of NS-MnO_2. B) TEM image of δ-MnO_2 nanosheets (the inset shows the thickness of the nanosheets). C) HRTEM image of δ-MnO_2 nanosheets (the inset shows the SAED pattern). D) AFM image and E) the corresponding height profiles of δ-MnO_2 nanosheets (the numbers of 1, 2, and 3 correspond to the line scan number in (D). F) EDX maps of δ-MnO_2 nanosheets.

(Figure 2C; Table S1, Supporting Information). The Mn EXAFS spectra for δ-MnO_2 show two peaks in *R*-space spectra corresponding to the first Mn—O and Mn—Mn shells, respectively. As can be seen, the Mn—O and Mn—Mn peaks for NS-MnO_2 are weaker than the corresponding peaks for Bulk-MnO_2. Table S1 (Supporting Information) reveals that when the MnO_2 sheet thickness is of atomic length scales, as is the case for NS-MnO_2, the Mn—O coordination number (4.9) and Mn—Mn coordination number (5.4) are significantly reduced compared to the corresponding values for Bulk-MnO_2 (both 6.0). The data provide strong evidence for the existence of V_o in NS-MnO_2. Additionally, for NS-MnO_2 the Mn—O distance was smaller (1.89 Å) and the Mn—Mn distance larger (2.89 Å) than the corresponding values for Bulk-MnO_2 (1.90 and 2.88 Å, respectively), which indicates a structural distortion of some sort exists in the ultrathin nanosheets. Xie and co-workers reported the coexistence of V_{Mn} and V_o in monolayered MnO_2.[12a] The existence of single-V_{Mn} or both V_{Mn} and V_o may be not possible in our system, owing to the synthesis method used here. Instead, the V_o in the nanosheets gives rise to coordinatively unsaturated Mn sites, as evidenced by the XANES and EXAFS data above and further characterization studies below.

X-ray photoelectron spectroscopy (XPS) and UV–vis spectroscopy were used to examine the valence state of Mn in NS-MnO_2. The XPS survey spectrum for NS-MnO_2 showed the presence of Ni, Mn, O, K, and C, with the latter being due to adventitious hydrocarbons (Figure S5, Supporting Information). The elements identified by XPS were in good accord with EDX results (Figure S2, Supporting Information). Mn 2p XPS spectra (Figure S4B, Supporting Information) for NS-MnO_2 showed peaks at 653.46 and 641.91 eV (1:2 area ratio) due to Mn^{3+} ($2p_{1/2}$ and $2p_{3/2}$, respectively), and another set of peaks at 654.55 and 643.18 eV due to Mn^{4+} ($2p_{1/2}$ and $2p_{3/2}$, respectively).[17] The atomic ratio Mn^{3+}:Mn^{4+} was ≈0.59:1, which is slightly higher than that (0.51:1) of Bulk-MnO_2 (Figure S6, Supporting Information). UV–vis diffuse reflectance spectroscopy provided additional evidence for the existence of an Mn (III) species. A band at ≈380 nm and peaks originating from

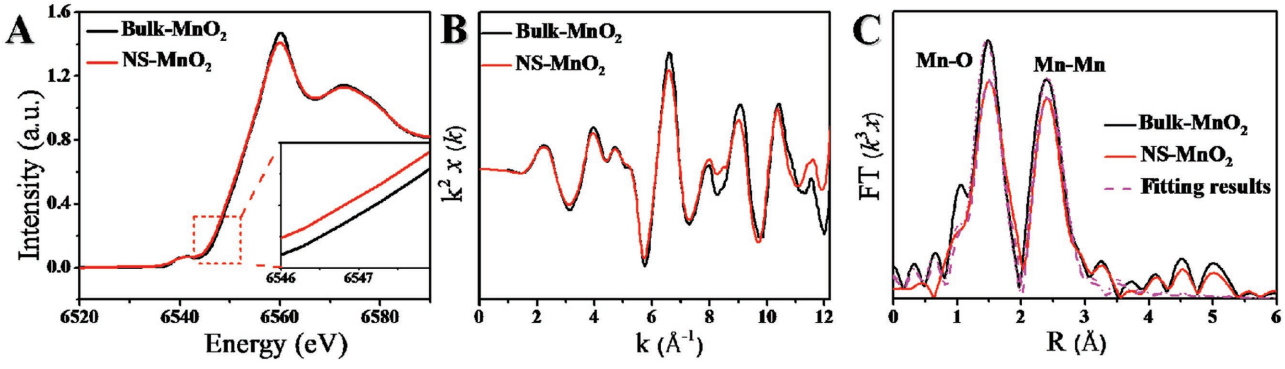

Figure 2. A) Mn K-edge XANES spectra. B) Mn K-edge EXAFS oscillation function $k^2\chi(k)$ and C) magnitude of k^2-weighted Fourier transforms of Mn K-edge EXAFS spectra for Bulk-MnO_2 and NS-MnO_2.

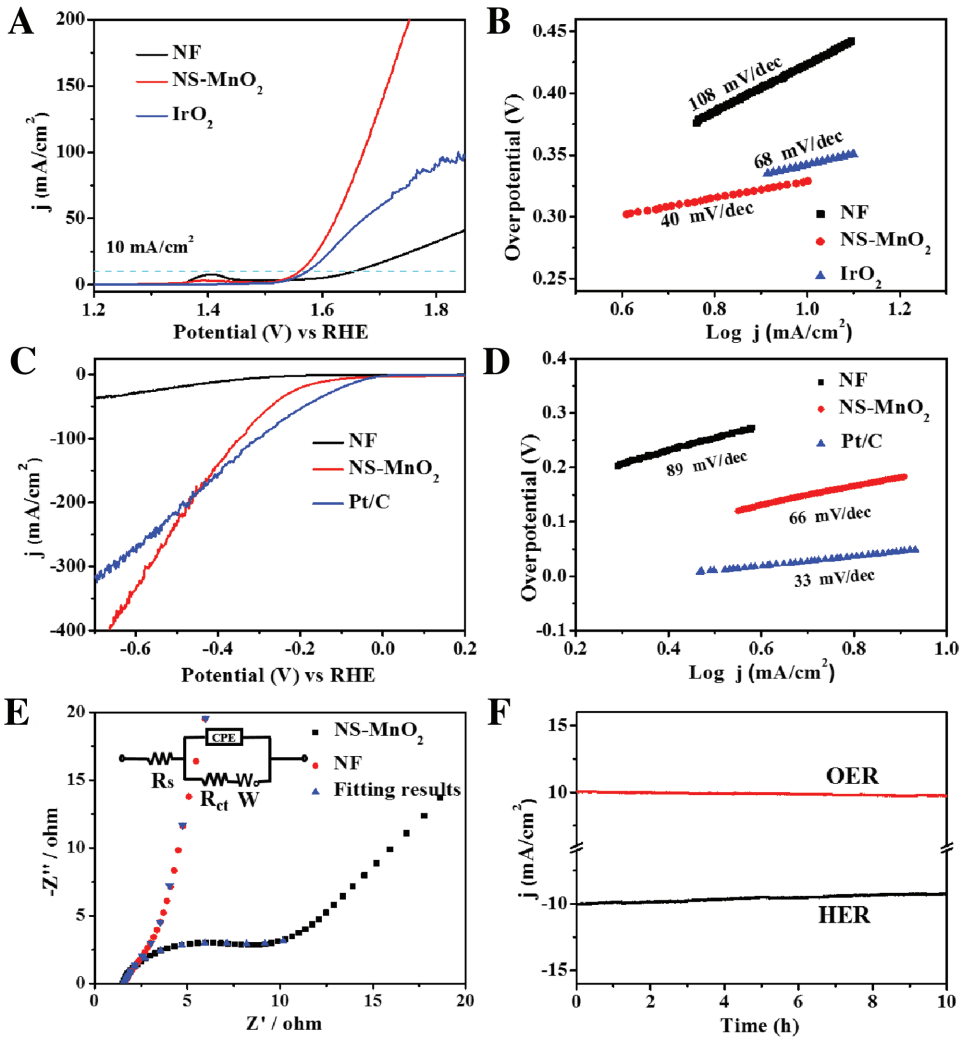

Figure 3. A) Linear sweep voltammetry (LSV) curves for OER at a scan rate of 5 mV s^{-1}. B) Tafel plots for OER. C) LSV curves for HER at 5 mV s^{-1}. D) Tafel plots for HER. E) Nyquist plots for NS-MnO_2 and NF (the inset shows the equivalent electrical circuit from the fitted impedance spectra). F) Current density versus time (*I*–*t*) curves of HER and OER for NS-MnO_2.

d–d transitions in the visible region are characteristic of Mn^{3+}, providing strong support for the presence of Mn^{3+} sites in NS-MnO_2 (Figure S7, Supporting Information).[13d,16] The high fraction of Mn^{3+} centers is associated with the abundance of V_o in NS-MnO_2. The unique 2D structure, V_o and Mn^{3+} sites in NS-MnO_2 were expected to dramatically alter its electronic and electrocatalytic properties for water splitting, as confirmed by experiments below.

Recently, δ-MnO_2 has been studied in relation to OER, but rarely in relation to HER. To evaluate the electrocatalytic activity of NS-MnO_2 for OER and HER, a three-electrode system was used (see the Supporting Information), and the performance of NS-MnO_2 compared against the NF, IrO_2, and commercial Pt/C electrocatalyst (20 wt% Pt). As shown in **Figure 3**A, all the catalysts showed water oxidation activity, with the first peak around 1.38 V (vs RHE) for the NF assigned to the oxidation of Ni^{2+}/Ni^{3+} mediated by OH^-.[17] NS-MnO_2 exhibited excellent electrocatalytic activity for OER with an overpotential (η) of 0.32 V at 10 mA cm^{-2}, much lower than that of NF (0.39 V) and IrO_2 (0.34 V). Moreover, the Tafel slope (Figure 3B) of NS-MnO_2 is 40 mV dec^{-1}, which was smaller than that of NF (108 mV dec^{-1}) and IrO_2 (68 mV dec^{-1}). By contract, Bulk-MnO_2 nearly did not exhibit any OER activity (Figure S8A, Supporting Information). The Faradaic efficiency of oxygen evolution on NS-MnO_2 was calculated and presented in Figure S9 (Supporting Information). Excellent agreement was found between the amount of O_2 evolved and that predicted by theory, suggesting that NS-MnO_2 exhibits nearly 100% Faradaic efficiency for catalytic OER at an overpotential of 400 mV. Results confirm that NS-MnO_2 demonstrates the best OER performance of the electrocatalysts tested, with its excellent activity relating to its unique 2D structure.

Currently, there is great interest in the discovery of low cost bifunctional electrocatalysts with excellent activity for both OER and HER, which would therefore satisfy requirements for overall water splitting. Thus, the performance of NS-MnO_2 toward electrochemical HER was also studied. As revealed in Figure 3C, NS-MnO_2 showed significantly enhanced

performance compared to pristine NF. At the same current density of 10 mA cm^{-2}, the overpotentials for H_2 evolution were 378 mV for NF and 196 mV for NS-MnO_2. Bulk-MnO_2 showed an overpotential of 757 mV and negligible HER performance (Figure S8B, Supporting Information). Furthermore, the overpotential for Pt/C at 300 mA cm^{-2} was 665 mV, which was higher than that of NS-MnO_2 (605 mV), direct evidence that HER performance of NS-MnO_2 was superior to that of Pt/C at high current densities. In order to gain deeper insight into the excellent HER activity of NS-MnO_2, NF, and commercial Pt/C, Tafel plots were constructed (Figure 3D), with slopes increasing in the order Pt (33 mV dec^{-1}) < NS-MnO_2 (62 mV dec^{-1}) < NF (89 mV dec^{-1}). Results suggest that NS-MnO_2 is also a promising HER electrocatalyst. To explain the differences in HER performance between Bulk-MnO_2 and NS-MnO_2, electrochemically active surface areas (EASAs) were determined by double-layer capacitance from the cyclic voltammetry (CV) curves. Figure S10A,B (Supporting Information) shows the typical CV curves for Bulk-MnO_2 and NS-MnO_2 collected at different scanning rates (5–40 mV s^{-1}). The EASA determined for Bulk-MnO_2 and NS-MnO_2 were 0.80 and 19.58 mF cm^{-2}, respectively (Figure S10C, Supporting Information), revealing the active surface area of NS-MnO_2 was ≈25 times higher than that of Bulk-MnO_2. The higher EASA for NS-MnO_2 reflects that ultrathin nanosheet architecture of samples. To the best of our knowledge, this is the first report on the excellent HER performance for δ-MnO_2 (η = 196 mV at 10 mA cm^{-2}) which arises in the case of NS-MnO_2 from modification of morphology and electronic structure. It is worth noting that the catalytic activity of NS-MnO_2 surpasses that of most reported bifunctional electrocatalysts (Table S2, Supporting Information). Hence, NS-MnO_2 represents one of the most promising electrocatalysts yet identified for overall water splitting.

It is well-known that electrical conductivity and transport resistances are major factors that influence electrocatalyst performance in overall water splitting. Thus, electrochemical impedance spectroscopy (EIS) studies were performed (Figure 3E) and the measured impedance data fitted and further analyzed by an equivalent electrical circuit (inset of Figure 3E), which consists of an electrolyte solution resistance (R_s), Warburg impedance (W), charge-transfer impedance (R_{ct}), and a constant phase element. The Warburg impedance can be estimated from the slope of the EIS curve in the low frequency region. It should be noted that the steeper slope of low-frequency line in Figure 3E results from the different surface of the electrode, implying a low diffusion resistance of the electrode.[18] The R_s values for the electrolyte solution was similar for both electrodes (1.62 and 1.54 Ω), with NS-MnO_2 possessing a slightly higher R_{ct} value (10.6 Ω) compared to NF (9.5 Ω). Results confirm that NS-MnO_2 has a high electrical conductivity and fast charge transfer rate, similar to that of the metallic Nickel foam.[19]

Electrocatalyst durability is also a critical factor for practical applications. The long-term cycling performance of NS-MnO_2 was measured at the current density of 10 mA cm^{-2} with overpotentials of 320 and 196 mV for OER and HER, respectively. As shown in Figure 3F, there was no obvious decrease in the current density after cycling for 10 h. No change in the morphology of NS-MnO_2 was observed after 10 h cycling (Figure S11, Supporting Information), further confirming the excellent durability of NS-MnO_2.

DFT calculations revealed the origin of the excellent electrocatalyst activity of NS-MnO_2 for overall water splitting. The crystal structure model of δ-MnO_2 consisted of brucite-like layers composed of edge-sharing MnO_6 octahedron (**Figure 4**A), with K^+ ions occupying sites in the interlayer region.[20] Figure S12 (Supporting Information) shows the effect of introducing a V_o into the slab of two-layered δ-MnO_2 (denoted as V_o-MnO_2), with an Mn^{3+} defect site existing next to the O vacancy. Figure S13 (Supporting Information) shows the band gap between valence band maximum and conduction band minimum in nondefective δ-MnO_2 (denoted as Pure-MnO_2), confirming semiconductor properties.[20b,21] Conversely, the total density of states (TDOS) and partial density of states (PDOS) calculated for V_o-MnO_2 is continuous near the Fermi level (E_F), suggesting a semimetal property for V_o-MnO_2 (Figure 4B). The continuous DOS near E_F is expected to impart V_o-MnO_2 with excellent electrical conductivity, efficient electron transport, and ion diffusion properties,[22] exactly what was determined experimentally for NS-MnO_2. Compared to the DOS calculated for metal nickel and the semiconductor NiO (Figure S14, Supporting Information), the electronic structure of V_o-MnO_2 is much more similar to metallic Ni, which also agrees with the EIS results (Figure 3E). Since electrocatalytic water splitting occurs on the surface of the catalyst, the adsorption behavior of H_2O on δ-MnO_2 is a key factor for water splitting.[23] Figure S15 (Supporting Information) shows the optimized adsorption structures of H_2O on the surface of Pure-MnO_2, V_o-MnO_2, NiO, and Ni. As summarized in Figure 4C, V_o-MnO_2 possessed the highest absolute H_2O adsorption energy (1.1 eV), significantly larger than values determined for Pure-MnO_2 (0.65 eV), NiO (0.38 eV), and Ni (0.71 eV). The results imply that the adsorption of H_2O on the surface of V_o-MnO_2 is energetically favored, thereby leading to faster charge transfer from the surface of V_o-MnO_2 to H_2O during the electrochemical reaction.

The adsorption free energy of H* (ΔG(H*)) is an important benchmark of HER activity for metal catalysts, with a smaller ΔG(H*) representing a better HER activity.[24] DFT calculations were thus carried out to determine ΔG(H*) for the various electrocatalysts tested in this study. The possible adsorption sites of H* on the different surfaces are depicted in Figure S16 (Supporting Information). Pure-MnO_2 (–0.7 eV) afforded a smaller ΔG(H*) than NiO (–0.638 eV) or Ni (–0.47 eV). After introducing V_o into MnO_2, the resulting sample V_o-MnO_2 gave the smallest ΔG(H*) (–0.134 eV). From a thermodynamics viewpoint, the chemical adsorption of H* on Pure-MnO_2, Ni and NiO is too strong for efficient electrocatalytic HER activity,[25] whereas the adsorption strength on V_o-MnO_2 is more ideal for efficient electrocatalytic HER (Figure 4D). Results strongly suggest that V_o-Mn^{3+} active sites on the surface of ultrathin δ-MnO_2 nanosheets may be highly beneficial to the HER activity.[26] In addition, in edge-sharing MnO_6 octahedra, Mn^{3+} is expected to be unstable due to the single electron in the e_g band (t_{2g}^3, e_g^1),[27] which may contribute to the excellent efficient HER performance. The HER could be envisaged to proceed via the oxidation of Mn^{3+} to Mn^{4+} (i.e., $Mn^{3+} + H_2O \rightarrow Mn^{4+} + 1/2H_2 + OH^-$). As reported by other groups,[13d,16,28]

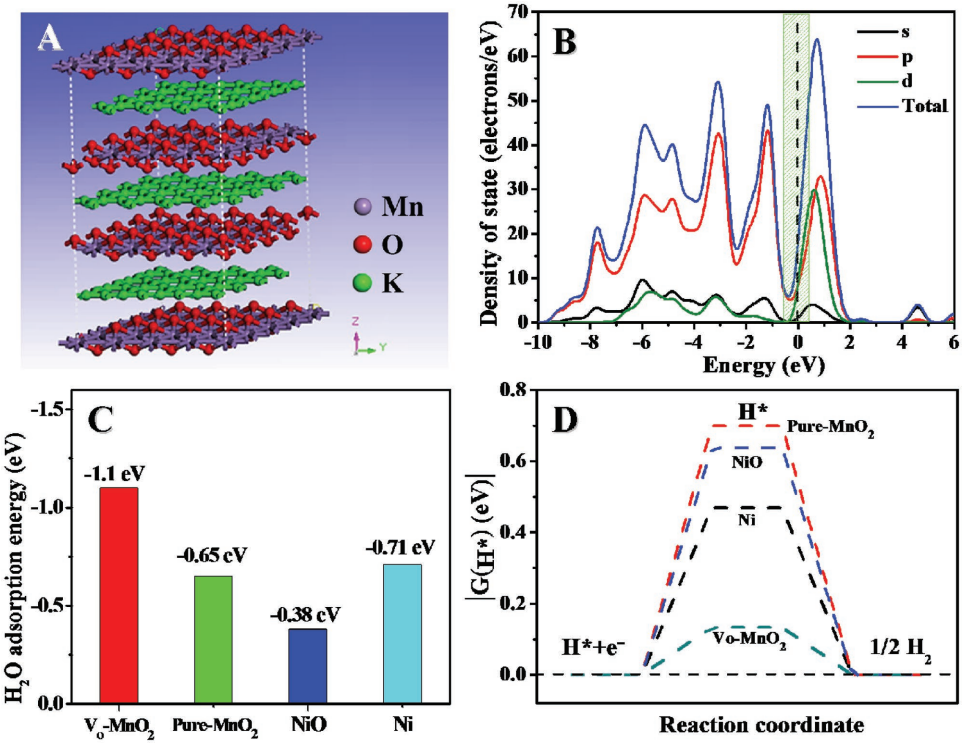

Figure 4. A) Crystal structure model of δ-MnO_2. B) TDOS and PDOS of V_o-MnO_2: the E_F is set at 0 eV. C) DFT-calculated adsorption energies for H_2O molecules on the surfaces of Pure-MnO_2, V_o-MnO_2, NiO, and Ni. D) Calculated free-energy diagram for hydrogen evolution over the surfaces of Pure-MnO_2, V_o-MnO_2, (110) surface of NiO and (200) surface of Ni at equilibrium potential.

under neutral conditions (pH = 7) MnO_2 exhibits poor activity and instability, due primarily to the instability of Mn(III) at neutral pH (Figure S17, Supporting Information). However, under alkaline conditions, the oxygen evolution mechanism of NS-MnO_2 ($4Mn^{3+} + 4OH^- \rightarrow 4Mn^{2+} + O_2 + 2H_2O$) would be highly preferred over the disproportionation reaction of Mn^{3+} to Mn^{2+} and Mn^{4+} during OER. Thus, the abundance of V_o in NS-MnO_2 created and stabilized defective Mn^{3+} active sites, and ultimately underpinned the excellent OER and HER performance of NS-MnO_2.

On the basis of the data presented above, the superior electrocatalytic performance of NS-MnO_2 for overall water splitting can be rationalized as follows: (1) The ultrathin nanosheet array architecture of NS-MnO_2 offers a very large EASA. The higher EASA provides an abundance of active sites for the HER and OER. (2) The numerous V_o results in the formation of unsaturated Mn^{3+} sites, which give NS-MnO_2 partial metallic character, high electrical conductivity, and improved charge-transfer properties, all of which contribute to excellent overall water splitting performance of NS-MnO_2.

In summary, atomically thin δ-MnO_2 nanosheet (1.4 nm) arrays have been successfully prepared through an in situ growth method. The obtained V_o-doped NS-MnO_2 offers an abundance of coordinately unsaturated Mn^{3+} sites that activate δ-MnO_2 for overall water splitting. Defect engineering gives NS-MnO_2 half-metallic character, promoting H_2O adsorption and leading to excellent HER and OER performance. This work highlights the untapped potential of 2D intercalation layer materials and defect engineering in the development of earth-abundant element electrocatalysts for overall water splitting.

Supporting Information

Supporting Information is available from the Wiley Online Library or from the author.

Acknowledgements

The authors are grateful for the financial support from the National Science Foundation of China (21377060, 51572270, U1662118, 51322213, 21401206, 21301183, and 21401207), the Science and Technology Infrastructure Program of Jiangsu (BM201380277), the Six Talent Climax Foundation of Jiangsu (20100292), the "333" Outstanding Youth Scientist Foundation of Jiangsu (C2011015), the Key Project of Environmental Protection Program of Jiangsu (2013016), the Priority Academic Program Development of Jiangsu Higher Education Institutions (PAPD) sponsored by SRF for ROCS, SEM (2013S002), the Ministry of Science and Technology of China (2014CB239402 and 2013CB834505), the National Key Projects for Fundamental Research and Development of China (2016YFB0600900), the Strategic Priority Research Program of the Chinese Academy of Sciences (XDB17030300), and the Youth Innovation Promotion Association. Mn K-edge XAFS measurements were performed at the 1W1B beamline of Beijing Synchrotron Radiation Facility.

Conflict of Interest

The authors declare no conflict of interest.

Keywords

δ-MnO_2, bifunctional electrocatalysts, defects, overall water splitting, ultrathin nanosheet arrays

Received: January 1, 2017
Revised: March 23, 2017
Published online:

[1] M. S. Dresselhaus, I. L. Thomas, *Nature* **2001**, *414*, 332.
[2] a) R. Subbaraman, D. Tripkovic, K. C. Chang, D. Strmcnik, A. P. Paulikas, P. Hirunsit, M. Chan, J. Greeley, V. Stamenkovic, N. M. Markovic, *Nat. Mater.* **2012**, *11*, 550; b) X. Zou, Y. Zhang, *Chem. Soc. Rev.* **2015**, *44*, 5148; c) Y. Liu, G. Yu, G.-D. Li, Y. Sun, T. Asefa, W. Chen, X. Zou, *Angew. Chem., Int. Ed.* **2015**, *54*, 10752; d) X. Zou, X. Huang, A. Goswami, R. Silva, B. R. Sathe, E. Mikmeková, T. Asefa, *Angew. Chem., Int. Ed.* **2014**, *126*, 4461.
[3] Y. Zhang, Y.-W. Tan, H. L. Stormer, P. Kim, *Nature* **2005**, *438*, 201.
[4] V. Perebeinos, *Nat. Nanotechnol.* **2015**, *10*, 485.
[5] X. Zhang, J. Zhang, J. Zhao, B. Pan, M. Kong, J. Chen, Y. Xie, *J. Am. Chem. Soc.* **2012**, *134*, 11908.
[6] F. Song, X. Hu, *Nat. Commun.* **2014**, *5*, 4477.
[7] a) X. Huang, S. Tang, X. Mu, Y. Dai, G. Chen, Z. Zhou, F. Ruan, Z. Yang, N. Zheng, *Nat. Nanotechnol.* **2011**, *6*, 28; b) K. Ariga, Q. Ji, J. P. Hill, Y. Bando, M. Aono, *NPG Asia Mater.* **2012**, *4*, e17; c) Y. Sun, Z. Sun, S. Gao, H. Cheng, Q. Liu, J. Piao, T. Yao, C. Wu, S. Hu, S. Wei, *Nat. Commun.* **2012**, *3*, 1057.
[8] Y. Li, H. Wang, L. Xie, Y. Liang, G. Hong, H. Dai, *J. Am. Chem. Soc.* **2011**, *133*, 7296.
[9] Y. Zheng, Y. Jiao, Y. Zhu, L. H. Li, Y. Han, Y. Chen, A. Du, M. Jaroniec, S. Z. Qiao, *Nat. Commun.* **2014**, *5*, 3783.
[10] D. Voiry, M. Salehi, R. Silva, T. Fujita, M. Chen, T. Asefa, V. B. Shenoy, G. Eda, M. Chhowalla, *Nano Lett.* **2013**, *13*, 6222.
[11] C. Tang, H. S. Wang, H. F. Wang, Q. Zhang, G. L. Tian, J. Q. Nie, F. Wei, *Adv. Mater.* **2015**, *27*, 4516.
[12] a) H. Wang, J. Zhang, X. Hang, X. Zhang, J. Xie, B. Pan, Y. Xie, *Angew. Chem., Int. Ed.* **2015**, *54*, 1195; b) T. Yao, L. Liu, C. Xiao, X. Zhang, Q. Liu, S. Wei, Y. Xie, *Angew. Chem., Int. Ed.* **2013**, *52*, 7554.
[13] a) A. C. Thenuwara, E. B. Cerkez, S. L. Shumlas, N. H. Attanayake, I. G. McKendry, L. Frazer, E. Borguet, Q. Kang, R. C. Remsing, M. L. Klein, *Angew. Chem., Int. Ed.* **2016**, *55*, 10381; b) F. Cheng, T. Zhang, Y. Zhang, J. Du, X. Han, J. Chen, *Angew. Chem., Int. Ed.* **2013**, *52*, 2474; c) A. Bergmann, I. Zaharieva, H. Dau, P. Strasser, *Energy Environ. Sci.* **2013**, *6*, 2745; d) T. Takashima, K. Hashimoto, R. Nakamura, *J. Am. Chem. Soc.* **2012**, *134*, 1519.
[14] L. Chen, X. Dong, Y. Wang, Y. Xia, *Nat. Commun.* **2016**, *7*, 11741.
[15] K. Xu, P. Chen, X. Li, Y. Tong, H. Ding, X. Wu, W. Chu, Z. Peng, C. Wu, Y. Xie, *J. Am. Chem. Soc.* **2015**, *137*, 4119.
[16] K. Jin, H. Seo, T. Hayashi, M. Balamurugan, D. Jeong, Y. K. Go, J. S. Hong, K. H. Cho, H. Kakizaki, N. Bonnet-Mercier, M. G. Kim, S. H. Kim, R. Nakamura, K. T. Nam, *J. Am. Chem. Soc.* **2017**, *139*, 2277.
[17] Y. Gu, Z. Lu, Z. Chang, J. Liu, X. Lei, Y. Li, X. Sun, *J. Mater. Chem. A* **2013**, *1*, 10655.
[18] X. Dai, D. Chen, H. Fan, Y. Zhong, L. Chang, H. Shao, J. Wang, J. Zhang, C.-N. Cao, *Electrochim. Acta* **2015**, *154*, 128.
[19] Z. Shan, P. S. Archana, G. Shen, A. Gupta, M. G. Bakker, S. Pan, *J. Am. Chem. Soc.* **2015**, *137*, 11996.
[20] a) Y. Liu, Y. Qiao, W. Zhang, H. Xu, Z. Li, Y. Shen, L. Yuan, X. Hu, X. Dai, Y. Huang, *Nano Energy* **2014**, *5*, 97; b) K. D. Kwon, K. Refson, G. Sposito, *Phys. Rev. Lett.* **2008**, *100*, 146601.
[21] a) Y. Zhao, F. Teng, J. Xu, Z. Liu, Y. Yang, Q. Zhang, W. Yao, *RSC Adv.* **2015**, *5*, 100934; b) Y. Noda, K. Ohno, S. Nakamura, *Phys. Chem. Chem. Phys.* **2016**, *18*, 13294.
[22] S. Peng, L. Li, H. B. Wu, S. Madhavi, X. W. D. Lou, *Adv. Energy. Mater.* **2015**, *5*, 1401172.
[23] X. Jia, Y. Zhao, G. Chen, L. Shang, R. Shi, X. Kang, G. I. N. Waterhouse, L.-Z. Wu, C.-H. Tung, T. Zhang, *Adv. Energy. Mater.* **2016**, *6*, 1502585.
[24] J. K. Nørskov, T. Bligaard, A. Logadottir, J. Kitchin, J. Chen, S. Pandelov, U. Stimming, *J. Electrochem. Soc.* **2005**, *152*, J23.
[25] J. Greeley, T. F. Jaramillo, J. Bonde, I. Chorkendorff, J. K. Nørskov, *Nat. Mater.* **2006**, *5*, 909.
[26] L.-L. Feng, G. Yu, Y. Wu, G.-D. Li, H. Li, Y. Sun, T. Asefa, W. Chen, X. Zou, *J. Am. Chem. Soc.* **2015**, *137*, 14023.
[27] S. Lee, G. Nam, J. Sun, J. S. Lee, H. W. Lee, W. Chen, J. Cho, Y. Cui, *Angew. Chem., Int. Ed.* **2016**, *55*, 8599.
[28] a) K. Jin, A. Chu, J. Park, D. Jeong, S. E. Jerng, U. Sim, H. Y. Jeong, C. W. Lee, Y. S. Park, K. D. Yang, G. K. Pradhan, D. Kim, N. E. Sung, S. H. Kim, K. T. Nam, *Sci. Rep.* **2015**, *5*, 10279; b) D. Jeong, K. Jin, S. E. Jerng, H. Seo, D. Kim, S. H. Nahm, S. H. Kim, K. T. Nam, *ACS Catal.* **2015**, *5*, 4624.

